The effect of excitation wavelength on dynamics of laser-produced tin plasma

S. S. Harilal,[1] T. Sizyuk,[1] A. Hassanein,[1] D. Campos,[1] P. Hough,[2] and V. Sizyuk[1]
[1]*School of Nuclear Engineering and Center for Materials Under Extreme Environment, Purdue University, 400 Central Dr., West Lafayette, Indiana 47907, USA*
[2]*School of Physical Sciences and National Centre for Plasma Science and Technology, Dublin City University, Glasnevin, Dublin 9, Ireland*

(Received 19 September 2010; accepted 8 February 2011; published online 24 March 2011)

We investigated the effect of the excitation wavelength on the density evolution of laser-produced tin plasmas, both experimentally and numerically. For producing plasmas, Sn targets were excited with either 10.6 μm CO_2 laser or 1.06 μm Nd:yttrium aluminum garnet laser; both are considered to be potential excitation lasers for extreme ultraviolet lithography laser-produced plasma light sources. The electron density of the plasma during the isothermal expansion regime was estimated using an interferometric technique. The Stark broadening of isolated singly-ionized emission was employed for deducing the density during the plasma adiabatic expansion regime. Our results indicate that the excitation source wavelength determines the initial density of the plasma, as well the plume expansion dynamics. Numerical simulation using HEIGHTS simulation package agrees well with the experimentally measured density profile. © *2011 American Institute of Physics*. [doi:10.1063/1.3562143]

I. INTRODUCTION

Laser-produced plasmas (LPP) are formed by focusing the output pulse from a high-power laser onto a target. The plasmas formed are very hot, expand rapidly, and their characteristic parameters change with time and space.[1,2] Initially, the plasma expands isothermally through the duration of the laser pulse, and in later times the plasma expands adiabatically.[3] Currently, there are numerous applications for LPP in a wide variety of fields, including pulsed-laser deposition,[4] nanoparticles and cluster production,[5] light sources for extreme ultraviolet (EUV) lithography[6] and microscopy,[7] micromachining,[8] elemental sensors (laser-induced breakdown spectroscopy[9] and laser-ablation inductively coupled plasma mass spectrometry[10]), laser propulsion,[8] simulation of astrophysical objects,[11] etc. A fundamental understanding of LPP is absolutely necessary for optimizing the LPP for various applications. Typically, the plasmas are characterized by their density and temperature, and most of the other properties of the plasma (emission, absorption, opacity, expansion dynamics, etc.) are closely related to these two basic parameters.[12]

Currently, much effort is being devoted to developing an efficient and debris-free LPP source at 13.5 nm for the next generation extreme ultraviolet lithography (EUVL).[6,13] Sn is considered to be the target of interest for producing this kind of plasmas, as its plasma emits strongly in the EUVL in-band region (13.5 nm with 2% bandwidth), contributed by various ionic stages (Sn^{8+}– Sn^{14+}).[14] However, the net release of 13.5 nm radiation by the plasma is related to plasma opacity, which depends on level populations of different ionic states, ionization balance, and electron density. The density of the plasma is governed by both laser and target properties. Typically, for nanosecond LPP, the leading edge of the laser creates plasma, and the remaining part of the laser heats the plasma instead of interacting with the target. The efficiency of laser-plasma coupling depends on the plasma frequency given by $\upsilon_p = 8900\sqrt{n_e}$, where n_e is the electron density in cm^{-3} and υ_p is in Hz. The reflection of the laser photons by the plasma takes place when the laser frequency is smaller than plasma frequency.

For obtaining the highest conversion efficiency (CE), i.e., the conversion from laser to EUV in-band radiation for an EUV source, ideal plasma temperatures and densities should be created for the longest possible period of time with the maximum size.[15] Many previous studies have shown that the EUV emission characteristics of laser-produced Sn plasmas strongly depend on laser and target parameters.[14,16–22] The main laser parameters that affect the efficiency of EUV light sources include laser wavelength,[23] pulse duration,[16] intensity,[18] spot size,[24] focusing geometry,[25] etc. Currently, two laser sources are considered for EUV plasma source production, viz, Nd:yttrium aluminum garnet (Nd:YAG) (1.06 μm) or CO_2 (10.6 μm).[23] The plasmas produced by both 1.06 and 10.6 μm radiate efficiently in the in−band radiation when they posses temperature in the ~30–50 eV range.[15] However, the CO_2 gas laser typically provides very high wall-plug efficiencies compared to flash-lamp pumped Nd:YAG lasers. Moreover, 10.6 μm excitation provides higher conversion efficiency (CE ~3%) as well as a narrower unresolved transition array (UTA) profiles due to lower opacity of the plasma.[14,24] Nd:YAG LPP provides[19] broader UTA with an in-band CE ~2%. The major difference between these plasmas lies in the evolution of their densities, both temporally and spatially.

The electron density constitutes one of the most fundamental parameters of plasmas, and for many plasma systems, varies more rapidly compared to any other plasma parameters, for example, electron temperature (T_e). However, it is often difficult to estimate the electron density accurately for

 © 2011 American Institute of Physics

Downloaded 30 Mar 2011 to 128.46.102.183. Redistribution subject to AIP license or copyright; see http://jap.aip.org/about/rights_and_permissions

LPP, as it varies several orders during plasma expansion. Although there exist several methods for estimating plasma density, each method has its own limitations.[26] As an example, optical emission spectroscopy (OES) is considered to be one of the easiest methods to estimate basic parameters of the plasma.[27] However, employing visible spectroscopy at the earliest time of plasma evolution (<50 ns) is rather difficult because of the presence of strong continuum emission. Interferometry employing visible laser light to probe the LPP is a versatile technique when the refractive index gradients caused by the plasma is moderately high (10^{18}–10^{20}/cm^3).[24] However, this technique fails when the densities are very low, or when they approach critical density of the probe beam.[28] Thomson scattering is probably the most accurate method, but a lot of effort is necessary to separate the scattered signal from the strong background noise. A Langmuir probe provides space averaged densities of LPP at later time.[29] Hence, no plasma diagnostic method is currently capable of mapping the complete spatial and temporal evolution of an expanding LPP electron density. A combination of two or more methods will be useful for achieving this task.

In this article, we investigated the excitation wavelength dependence (1.06 and 10.6 μm) of the evolution of the electron density of Sn plasma with a very high spatial and temporal resolution. Both wavelengths used in the present investigation are considered to be potential excitation lasers for EUVL light source and a systematic comparison of their plasma densities will provide more insight into expansion dynamics, photon transport, plasma absorption and reflection, debris emission, etc. Optical interferometry is used to estimate the density of the plasma during the plasma production. Stark broadening employing 2D spectral imaging is employed for estimating the density at a high spatial resolution and radially-integrated emission spectroscopy is utilized for obtaining electron densities at a specific point with a high temporal resolution. A special emphasis is also given for the accuracies and/or limitations of the plasma diagnostic tools used in the present studies. We also utilized the High Energy Interaction with General Heterogeneous Target Systems (HEIGHTS) simulation package[25,30] for calculating the density and temperature evolution of the plasma produced by Nd:YAG and CO_2 lasers.

II. MODELING RESULTS

HEIGHTS package has been developed over the last 20 years and is a set of multipurpose, multiphase, multidimensional computational tools that integrate heat transfer, thermal hydraulics, magneto-hydrodynamics, atomic and plasma physics, photon transport, and material erosion processes.[31] Currently, HEIGHTS package has numerous integrated models including 3D laser energy deposition and material bulk thermal response, surface melt-layer formation and movement, 3D gas and plasma magnetohydrodynamics, and 3D line and continuum photon radiation transport.[31] We utilized HEIGHTS in this study for modeling the density and temperature evolution of CO_2 and Nd:YAG produced plasmas.

Based on the developed physical and mathematical models, HEIGHTS allows the complete simulation of LPP evolution and EUV production. The built-in Monte Carlo models for the laser energy deposition and radiation transport in the entire energy range consider the details of the absorbed, reflected, reabsorbed, and transmitted photons, as well as areas of most intensive absorption and heating. The laser absorption by a target is treated in three phases: first by the cold, unperturbed solid/liquid target, second by the target vapor, and then by the produced plasma layer. For accurate modeling of the above-described processes we calculated absorption/reflection coefficients for the first phase from the available experimental optical properties for laser reflection from liquid tin.[32,33] For modeling laser absorption in vapor material we used the approximation given by Grigoryan *et. al*.[34] As it is shown here, one of the main features of the collision-induced absorption is a quadratic dependence of the absorption coefficient on the density and a weak dependence on the temperature.[35] Based on this model, we calculated the absorption coefficient in the target vapor up to 0.7 eV and fitted the dependence between the experimental data for the liquid target and the Bremsstrahlung coefficient given by Johnston and Dawson.[36] The implemented model for tin target vaporization is based on the kinetics of evaporation which establishes the connection between the surface temperature and the net atom flux leaving the surface taking into account the possibility of recondensation.[37] The detailed description of laser energy absorption, vaporization/sublimation processes, and using very fine target surface mesh are very important for accurate comparative study of plasma properties/laser wavelengths needed in this study. The minimum cell size used at the surface is 0.1 μm. More details of HEIGHTS package can be found in recent publications.[15,25]

The temporal profiles of our Nd:YAG and CO_2 lasers used for the modeling studies are given in Fig. 1. The laser profiles were recorded using a Si photodiode and a multiple junction photovoltaic detectors, both possessing a rise time <1 ns. As shown in Fig. 1, the Nd:YAG pulse followed a Gaussian profile with 6 ns full width half maximum (FWHM), while the CO_2 laser profiles showed a spiky

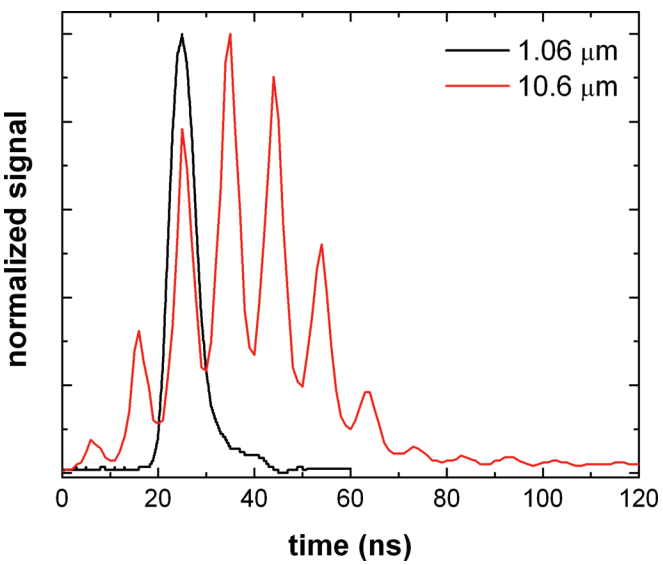

FIG. 1. (Color online) Normalized temporal profiles of Nd:YAG and CO_2 lasers used in the present studies.

Downloaded 30 Mar 2011 to 128.46.102.183. Redistribution subject to AIP license or copyright; see http://jap.aip.org/about/rights_and_permissions

structure with an approximately 30 ns FWHM. The intensities used for the present studies were 6×10^{10} W/cm^2 and 6×10^9 W/cm^2, respectively, and the same spot size (225 μm) was used for both wavelengths of illumination. The spot size was estimated using EUV pinhole camera by measuring EUV emitting region. The selection of the laser intensity is based on the fact that these are the laser intensities for producing the brightest EUV emission in the inband region (13.5 nm with 2% bandwidth). We measured an in-band CE of 2% and 3% for 1.06 and 10.6 μm radiation, respectively, under these irradiation conditions.[24,38]

The electron density and temperature distribution of the plasmas produced by Nd:YAG and CO_2 lasers using HEIGHTS at various times during the plasma evolution is shown in Figs. 2 and 3, respectively. The equal density contours (dotted lines in the figures) are given in cm^{-3} where the reported numbers indicate the powers of 10. These studies show that both plasmas are heated up to 30–50 eV during

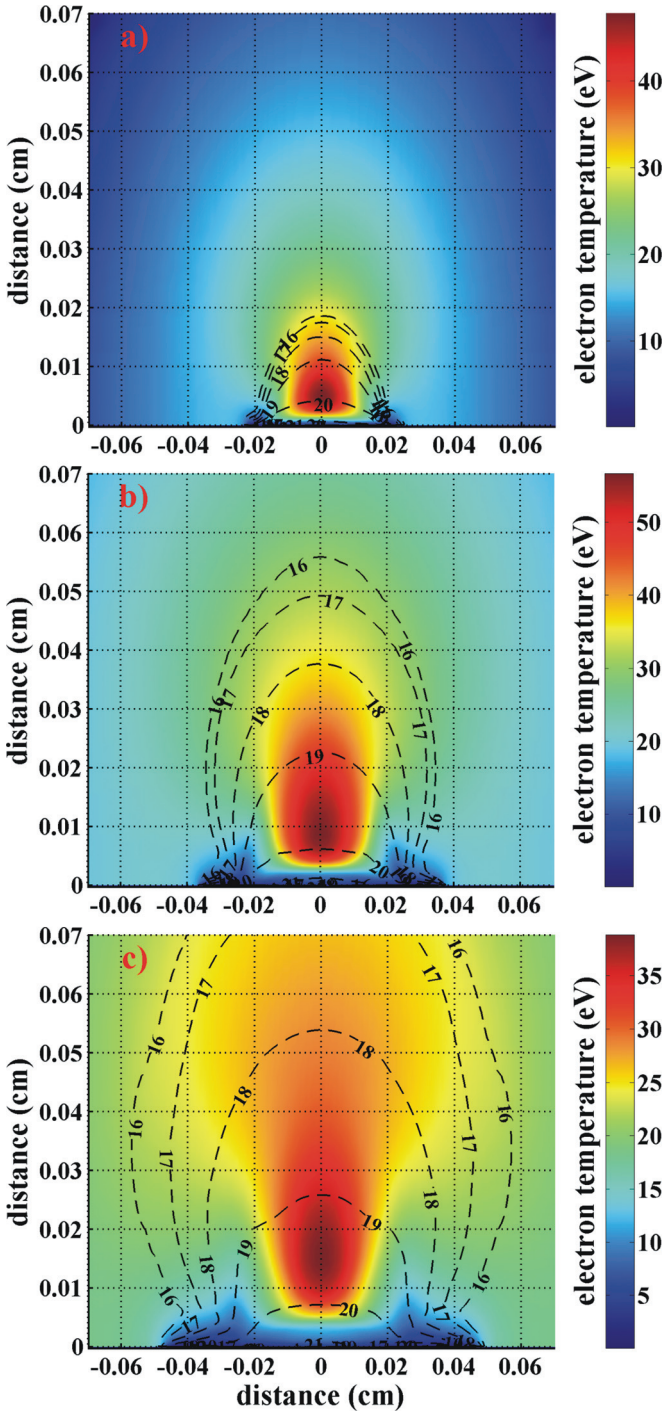

FIG. 2. (Color online) HEIGHTS temporal and spatial evolution of the temperature and density of a Nd:YAG produced Sn plasma. The photos correspond to times of (a) −3 ns, (b) 0 ns, and (c) 3 ns, where 0 ns correspond to the peak of the laser pulse.

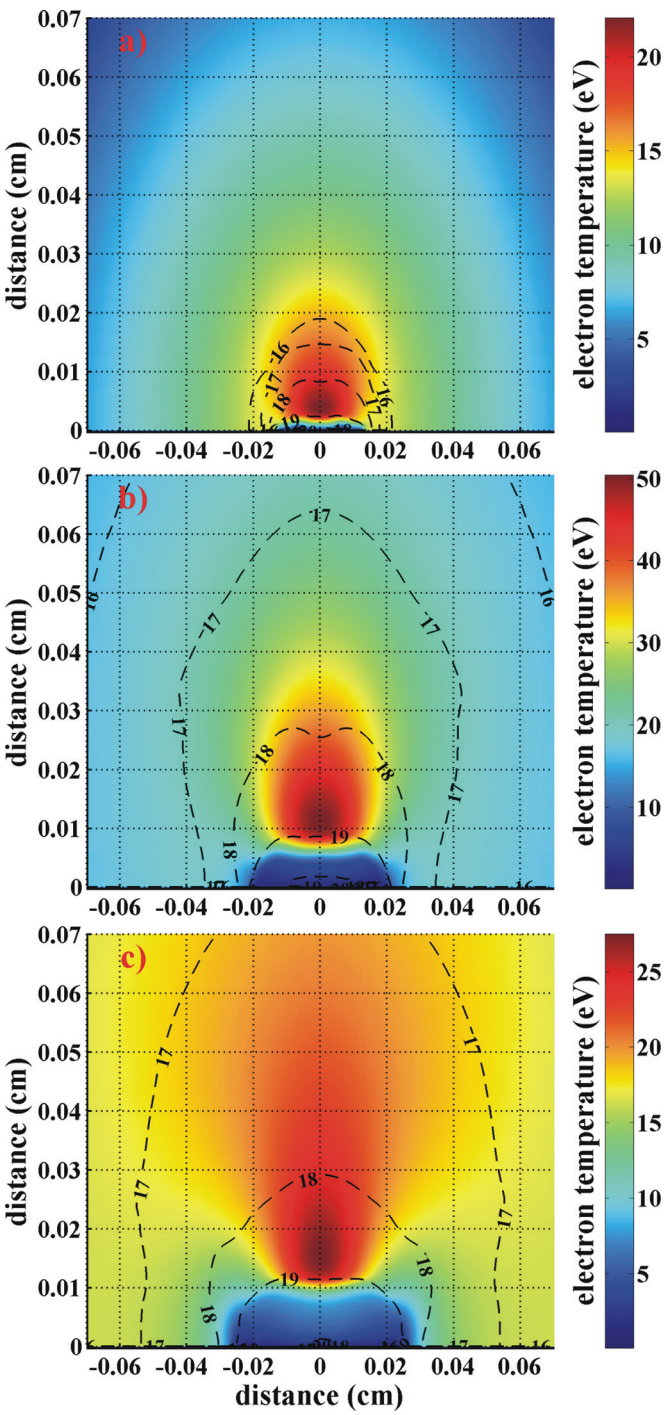

FIG. 3. (Color online) HEIGHTS temporal and spatial evolution of the temperature and density of a CO_2 produced Sn plasma. The photos correspond to times of (a) −15 ns, (b) 0 ns, and (c) 15 ns, where 0 ns correspond to the peak of the laser pulse.

Downloaded 30 Mar 2011 to 128.46.102.183. Redistribution subject to AIP license or copyright; see http://jap.aip.org/about/rights_and_permissions

the laser pulse. However, the density values showed considerable differences between the two lasers. For the Nd:YAG plasma, the density reaches the critical value soon after irradiation and the laser absorption region is moved to ~10 μm above the target surface at the peak of the laser pulse. For the CO_2 excited plasma, the front of the laser absorption region is further away from the target surface (>50 μm at the peak of the laser pulse) due to a critical density two orders of magnitude less than the critical density of the Nd:YAG beam.

III. EXPERIMENTAL DETAILS

The schematic of the experimental setup is given in Fig. 4. For producing plasmas, 1.06 or 10.6 μm radiation from a Nd:YAG laser (6 ns FWHM) or CO_2 laser (30 ns FWHM) are used and temporal profiles of these lasers are given in Fig. 1. We utilized a plasma shutter device to chop the long tail of transversely excited atmospheric (TEA) CO_2 laser.[39] A combination of a wave plate and a cube polarizer was used for adjusting the energy of the 1.06 μm pulse. The mirror reflecting the 1.06 μm radiation is placed on a flip mount so that it can be conveniently removed from the 10.6 μm beam path. The lasers were focused onto planar Sn target positioned at the center of a vacuum chamber with a base pressure of $\sim 10^{-6}$ Torr, using a f/40 fused silica plano-convex lens for 1.06 μm, or a f/10 ZnSe meniscus lens for 10.6 μm.

A polarization-based Nomarski interferometer is used for recording the density profiles of the plasmas. A frequency doubled Nd:YAG laser is used as the probe laser, which was operated at 0.532 μm with a 5 ns FWHM and 1 cm in beam diameter. A $\lambda/2$ wave plate and a cube polarizer are used for adjusting the polarization and energy of the probe beam. The probe beam passes through the plasma parallel to the target surface, and the target is imaged onto the detector using f/10 lens. A Wollaston prism is inserted in front of the detector. A polarizer, oriented either parallel or perpendicular to the 45° incident polarization, is placed in between the Wollaston prism and the detector, so that the transmission is the same for both polarizations, and the two beams will interfere at the detector plane. A 532 nm bandpass filter is positioned in front of the camera (7.6 mm × 6.6 mm aperture area with a unit pixel size of 4.65 μm × 4.65 μm) to ensure that only the light from the interferometer laser is detected by the camera. The spatial resolution of the system is determined only by the quality of the imaging lens, and can therefore reach very high values. The time resolution of the interferometer setup is governed by the probe laser pulse width.

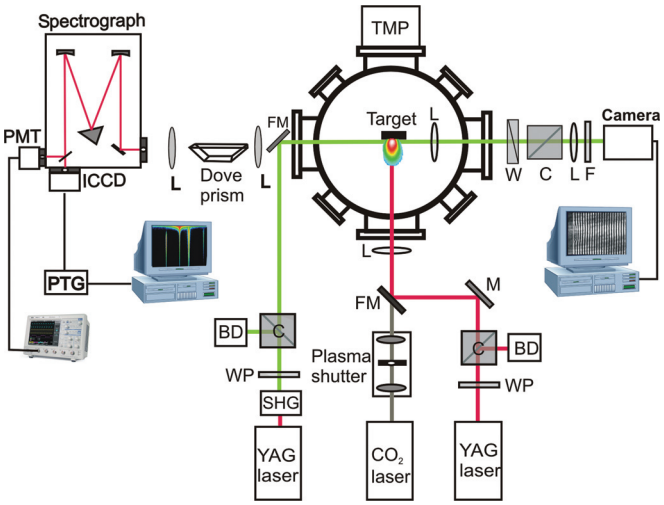

FIG. 4. (Color online) Schematic of the experimental setup (SHG, second harmonic generator; WP, wave plate; C, cube polarizer; BD, beam dump; L, lens; FM, flip mirror, M, mirror; W, Wollaston prism; F, filter; TMP, turbomolecular pump).

OES is utilized for estimating the density at later times with a high spatial and temporal resolution. For performing OES, the light emitted from the luminous plasma is transmitted through a quartz window mounted orthogonally to the direction of the plume expansion. An optical system is used to image the plasma plume onto the entrance slit of a 0.5 m spectrograph, so as to have a one-to-one correspondence with the sampled area of the plume and the image. By translating the optical system along the direction of target normal, spatiotemporal information about the plume's emission could be detected. One of the exit ports of the spectrograph was coupled to an intensified charged coupled device (ICCD, PI MAX 1024 × 1024 pixels, 13 μm pixels) and the other exit port was coupled to a photomultiplier tube (PMT, 2 ns rise time). Plasma density was estimated from the Stark broadened profiles of isolated lines, which were recorded using an 1800 g/mm holographic grating. The measured maximum resolution of our spectrograph with an 1800 g/mm grating using a He-Ne laser is 0.025 nm for a slit width of 15 μm. A programmable timing generator was used to control the delay time between the laser pulse and the ICCD camera with an overall temporal resolution of 1 ns. A Dove prism was inserted into the optical path for rotating the plasma image by 90° and 2D spectral imaging studies were performed by operating the ICCD in the imaging mode. The 2D spectral imaging technique provides a very high spatial resolution both in plume expansion and lateral directions.

IV. RESULTS AND DISCUSSION

The dynamic transient behavior of LPP is always challenging for diagnostics, since the fundamental plasma quantities vary dramatically with time and space. We utilized Nomarski interferometry to extract the density information of the plasma at the earliest time of plasma evolution.[28] The fringe shifts induced by LPPs produced by 1.06 and 10.6 μm lasers due to density gradients in the plasma at the end of the laser pulse is given in Fig. 5. The laser intensities used for producing plasmas were 6×10^{10} W/cm^2 and 6×10^9 W/cm^2, respectively, and the same spot size were used for both wavelengths of illumination (225 μm).

The maximum electron density measurable with interferometry is limited to the critical density of the plasma that relates to the probe laser wavelength. However, when the plasma density approaches the critical density, refraction and opacity effects significantly limit these diagnostics. The recorded interferogram clearly shows the plasma produced by the Nd:YAG laser reached critical density of the probe beam (3.5×10^{21}/cm^3) near the target at the peak of the laser pulse, and the critical density region is propagated to a

Downloaded 30 Mar 2011 to 128.46.102.183. Redistribution subject to AIP license or copyright; see http://jap.aip.org/about/rights_and_permissions

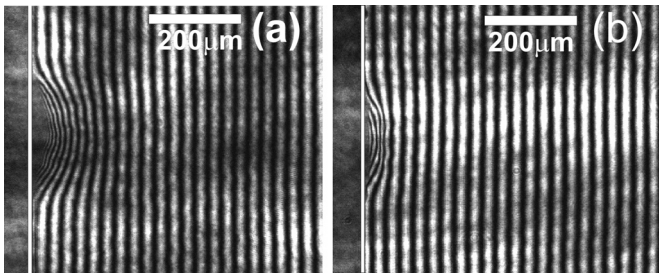

FIG. 5. Recorded interferogram for (a) Nd:YAG and (b) CO_2 produced plasmas at the end of the laser pulse. Interferograms clearly show the plasma generated by the Nd:YAG laser reaches the critical density of probe beam.

distance of nearly 100 μm from the target surface. However, the fringe shifts in the CO_2 LPP are visible even at very close distances from the target surface.

The electron density profile of LPP can be calculated for a relative fringe using the Abel inversion[40]

$$n_e \cong -\lambda n_c \int_r^{r_{\max}} \frac{d\varphi}{dx}(x^2 - r^2)^{-1/2} dx, \qquad (1)$$

where λ is the wavelength of the probe laser, n_c is the critical density of the plasma at the probe wavelength, φ is the phase shift, and r is the radial plasma coordinate.[28] Interferograms were analyzed using the IDEA software package[41] and an axial symmetry is assumed. The estimated density profiles of plasma generated by 1.06 and 10.6 μm radiation both at the peak and at the end of the laser pulse are given in Figs. 6 and 7, respectively. Both of the interferograms were recorded with an integration time equal to the probe laser pulse width.

The estimated maximum n_e of 1.06 μm LPP is 4.5×10^{20}/cm^3 at the peak of the laser pulse and at a distance of 100 μm from the target. The density profile obtained at

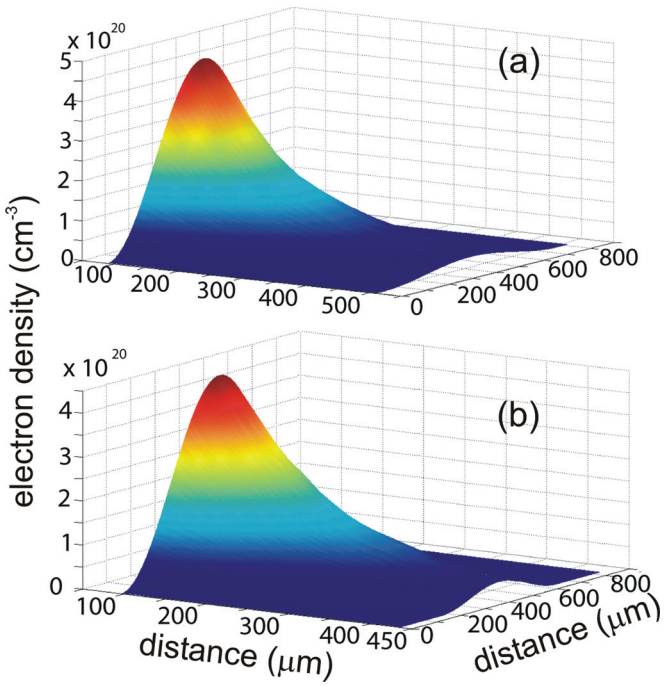

FIG. 6. (Color online) Density plot of the Nd:YAG LPP (a) at the peak and (b) at the end of the laser pulse.

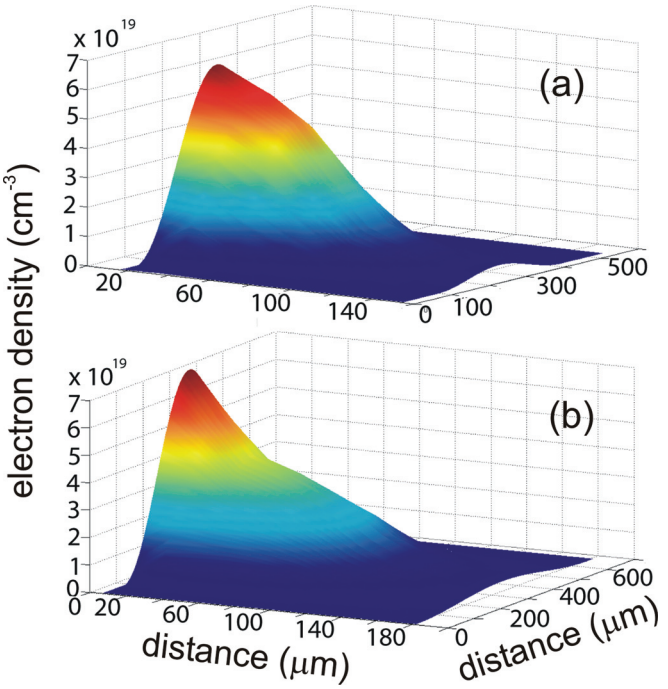

FIG. 7. (Color online) The density plot of the CO_2 LPP (a) at the peak and (b) at the end of the laser pulse.

the end of the laser pulse (4 ns after the peak) showed a slightly lower peak density though the density profiles showed hardly any difference. However, the density profiles obtained from a CO_2 LPP at the peak and at the end of the laser pulse showed considerable differences in the spatial profiles. These changes are partly due to the time duration of the pulses used in the present experiments (6 ns FWHM for 1.06 μm and 30 ns FWHM 10.6 μm) and the relatively long integration time of the probe beam (5 ns FWHM) relative to the 1.06 μm pulse width. The peak density value obtained with a 10.6 μm beam at the peak and end of the pulse is $\sim 6 \times 10^{19}$/cm^3. However, the density gradients are found to be steeper further away from the target at the peak of the laser pulse compared to the one recorded at the end of the laser pulse. This is profoundly caused by plasma expansion and movement of the laser absorption front as noticed in the modeling studies. The estimated peak densities showed a good agreement with HEIGHTS predictions. The disagreement noticed in the spatial distribution of the density could be caused by lack of time-resolution in the interferometry setup (probe pulse FWHM $\sim$5 ns).

LPP expansion is considered to be isothermal during the laser pulse and adiabatic after the termination of the laser pulse. During isothermal expansion a dynamical equilibrium exists between the plasma absorption and rapid transfer of thermal energy into kinetic energy, which controls the isothermal temperature of the plasma. During the isothermal expansion phase, the density of the plasma varies as[3]

$$n_e(x,y,z,t) = \frac{N_0 t}{2^{0.5}\pi^{1.5}\tau X(t)Y(t)Z(t)} \times \exp\left(-\frac{x^2}{2X(t)^2} - \frac{y^2}{2Y(t)^2} - \frac{z^2}{2Z(t)^2}\right), \qquad (2)$$

Downloaded 30 Mar 2011 to 128.46.102.183. Redistribution subject to AIP license or copyright; see http://jap.aip.org/about/rights_and_permissions

where N_0 is the total number of evaporated particles at the end of the laser pulse ($t = \tau$), and $X(t)$, $Y(t)$, and $Z(t)$ are the dimensions of the plasma when the density drops to 61% of the maximum density. The evaporated particle, or mass ablation from the target (in g/cm^2-s), is related to the wavelength of the laser through[42]

$$\dot{m} = 3 \times 10^3 I_a^{5/9} \lambda_l^{-4/9} N^{3/8}, \quad (3)$$

where I_a and λ_l are the excitation laser intensity in 10^{11} W/cm^2 and wavelength in μm, and N is the atomic number of the target. An estimate of mass ablation using the laser intensities used in the present studies showed that the Nd:YAG laser ablates >3 times the mass ablated by the CO_2 laser, which definitely affects the initial density of the plasma. This empirical formula calculation agrees well with the erosion estimate using HEIGHTS, which showed the depth of erosion by the CO_2 laser is about 0.3 μm, while in the case of the Nd:YAG laser, this value reaches about 1.1 μm under laser irradiation conditions for maximum EUV production.[15]

Also according to Eq. (2), the density of the plasma decreases exponentially with the distance from the target surface. We noticed a similar spatial decrease in density for 1.06 μm produced plasma (Fig. 6). However, the density of the 10.6 μm produced plasma showed a distinct nonisothermal expansion density profile (Fig. 7). This could be due to the longer pulse width of the CO_2 laser, along with a higher irradiation wavelength. The maximum recorded density near the target showed $\sim 6 \times 10^{19}$/cm^3, which is considerably larger than the critical density of the CO_2 pump beam (9×10^{18}/cm^3), and much lower than the probe laser critical density (3.5×10^{21}/cm^3). Hence, during the laser pulse, due to the plasma critical density, the absorption front moves away from the target surface. This was also confirmed by HEIGHTS simulation results which showed CO_2 laser absorption takes place in the expanding coronal region, while for Nd:YAG laser the deposition mainly takes place near the target surface, due to the higher critical density of the pump beam. This ascertains that most of the heating laser pulse is deposited efficiently in the plasma for a CO_2 LPP instead of depositing at the steep density profile observed with Nd:YAG LPP. This could lead to efficient heating of the plasma and hence higher CE as well as less debris from CO_2 LPP.[15,43]

The two orders of magnitude difference in early density will also affect the electron-ion thermalization time. The time of energy transfer among the electrons and ions τ_{ei} (s) is given by[44]

$$\tau_{ei} = \frac{3.5 \times 10^8 A T_e^{3/2}}{n_i \overline{Z}^2 \ln \Lambda}, \quad (4)$$

where A is the atomic weight in amu, $\overline{Z}$ is the average charge state, n_i is the ion density in cm^{-3}, and ln Λ is the Coulomb logarithm, which involves dynamic information about ion-electron collisions. The average charge-state of the ions emitted from a LPP can be calculated from the following equation:[45]

$$E(\text{eV}) = 5(\overline{Z} + 1) T_e, \quad (5)$$

where E is the most-probable ion kinetic energy, and T_e is in eV. Faraday cup analysis of ions emanating from LPP showed maximum probable kinetic energies of 1.2 and 2.2 keV respectively[23] for Nd:YAG and CO_2, which corresponds to $\overline{Z}$ of 8 and 14. Considering these average charge states and calculated ion densities at the peak of the laser pulse from the modeling tool, the estimated electron-ion thermalization time for Nd:YAG and CO_2 plasmas are 0.2 ns and 5 ns respectively. As the electron-ion thermalization time is much shorter than the Nd:YAG laser heating time, Nd:YAG LPP attains thermal equilibrium even at the earliest time of plasma evolution. On the other hand, because of inverse square dependence of τ_{ei} on charge state (Z), the CO_2 plasma ions are more efficiently heated by the laser.

Plasmas emit EUV radiation at 13.5 nm when the temperatures of the plasmas ~30–50 eV. Once plasma enters the adiabatic expansion regime, plasma cools very rapidly. Hence, the lifetime of EUV emission is restricted to excitation laser pulse width. During this time, densities are higher and interferometry is useful for estimating density plasma evolution. As time evolves, the density of the plasma decays very rapidly, and hence, the fringe shifts induced by the plasma refractive index gradient are negligible. Along with density, plasma temperatures also drop rapidly with time and in the later stages out-of-band emission, considering EUVL source perspective, in the UV and visible region dominate. Hence, in the later stages, we utilized OES for estimating density of the plasma. The major species contributing visible emission in the Sn plasma are excited neutral and singly ionic Sn.

The shape and width of the spectral lines emitted by plasmas are governed by collisional processes perturbing the emitting atoms and ions. We have selected the line-broadened profile of the Sn^+ transition at 645.4 nm ($6p^2P^o \rightarrow 6s^2S$) for the density measurements.[27] The 2D spectral imaging of the 645.4 nm line is given in Fig. 8 for plasmas produced by 1.06 μm and 10.6 μm laser radiation. Both the spectra were recorded in a time-integrated manner. Most of the previous spatially resolved density studies have been carried out by recording the intensity profiles at various distances from the normal of the target surface; on the other hand, the recorded

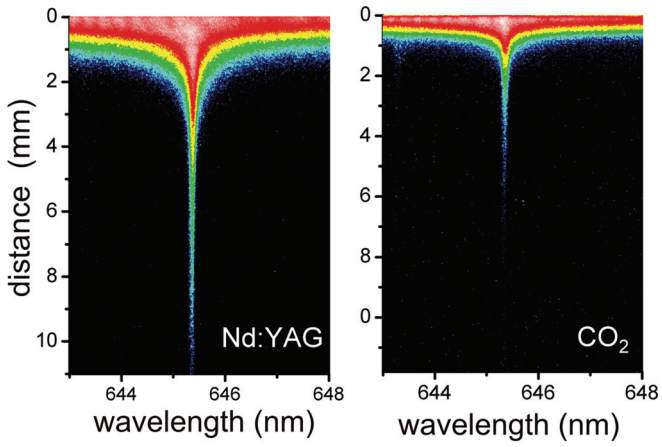

FIG. 8. (Color online) Stark-broadened profiles of Sn^+ lines at 645.4 nm from CO_2 and Nd:YAG laser-produced plasmas. These are 2D spectral images and recorded in a time integrated manner.

Downloaded 30 Mar 2011 to 128.46.102.183. Redistribution subject to AIP license or copyright; see http://jap.aip.org/about/rights_and_permissions

spectra were integrated along the line of sight.[27,46,47] It indicates, even though the recorded spectra are spatially resolved along the plume expansion axis, that they are spatially integrated in the radial direction. However, the 2D spectral imaging technique provides the spatial resolution near the size of the detector pixel size (for 1:1 plasma imaging onto the spectrograph slit).

Figure 8 clearly shows significant differences in the emission of the 645.4 nm line from Sn plasmas produced by 1.06 and 10.6 μm laser radiations. The extent of line emission and continuum emission is found to be higher for the Nd:YAG LPP. The spectral profiles obtained from shorter distances (<1 mm) clearly showed an asymmetry at the red wing. According to Griem,[48] the Stark profile that accounts for both the electron and ion Stark effects is represented by an asymmetric line given by the following expression:

$$j(x) = \frac{1}{\pi}\int_0^{\infty} \frac{W_R(\beta)}{1 + (x_t - \alpha^{4/3}\beta^2)^2} d\beta, \qquad (6)$$

where $W_R(\beta)$ is the ion microfield distribution function, β is the reduced field strength, α is the static ion-broadening parameter, and x is the reduced wavelength represented by $x_t = \pm(\lambda - \lambda_0 - d_e)/w_e$ (where λ_0 is peak wavelength of unperturbed emission, d_e and w_e are the electron impact Stark shift and width). The FWHM of Stark broadened profile for singly ionized line emission can then be approximated as[48]:

$$\Delta\lambda_{1/2} \approx 2\frac{w_e n_e}{10^{17}} + 3.5\alpha(1 - 1.2R)\frac{w_e n_e}{10^{17}} nm, \qquad (7)$$

where R is the ratio of the mean distance between ions to the Debye radius, which corresponds to $R = 8.98 \times 10^{-3} n_e^{1/6} n_e^{(-1/2)}$ (where n_e is in m^{-3} and T_e is in K). The first term on the right side of Eq. (7) represents the broadening due to electron contribution and the second term is the ion contribution. Equation (7) is valid[48] for $R \leq 0.8$ and $0.05 \leq \alpha \leq 0.5$. The α becomes zero when the line broadening contribution from micro-ion fields are negligible, when the line profile is represented by a Lorenzian profile. Based on previous reports, the major broadening factor for LPP is Stark, and is indicated by either a Lorenzian or Voigt line profiles.[49–51] Previous reports showed that line profiles emitted by highly charged ions in dense LPP display strong asymmetries in the red wing.[52–54] The factors that introduce asymmetry into the spectral profile are the ion-quadrupole interaction, the quadratic Stark effect, and fine structure splitting.

The spatial and temporal inhomogeneities of the expanding plasma may lead to asymmetrical profiles, due to the large variations in these parameters with space and time.[54] Spatial inhomogeneity is ruled out in our work, as the spatial resolution of recorded spectra are extremely high (<20 μm in the plume expansion direction and 15 μm in the radial direction). However, the recorded spectra are time-integrated, and hence, the inhomogeneities caused by temporal mixing cannot be ruled out. In order to confirm this, we recorded the Stark broadened profiles at 1 mm from the target surface at various times of evolution with a gate width of 10 ns, and the recorded spectra show similar asymmetry at earlier times. Hence, we attribute the asymmetries in the red wing of the profile could be influenced by ion micro fields. Using Eq. (7), we estimated the ion contribution in the broadened spectral line profile. The experimental R values ranged from 0.3 to 0.4. Using the approximation of $\alpha = 0.2$, the ion correction factor reaches a maximum value of 0.2 nm, which accounts for ~20% when compared to the broadening caused by the electron field at close distances to the target. Also, as the 2D spectral images and Stark broadened profiles showed, the influence of micro-ion fields on the line broadening is limited only at short distances and at very early times. At higher distances ($\geq$1 mm) and at later times ($\geq$100 ns), the ionic broadening contribution is found be negligible, as indicated by symmetric Stark broadened profiles.

The estimated time-integrated densities from the Stark broadened profiles are given in Fig. 9. Error bars are assigned based on the uncertainties caused by the asymmetries in both the profiles and the impact parameters. The smooth curves in Fig. 9 represent HEIGHTS simulation results. The results showed reasonably good agreement with experimental values, both in trend and estimated values. As expected the electron density of the Nd:YAG LPP is consistently higher than the CO_2 LPP especially at distances <4 mm. However, the reduction in density is found to be considerably faster in the case of 10.6 μm compared to 1.06 μm. The spatial dependence of electron density for 1.06 μm excitation approximately follows 1/z dependence, while the CO_2 LPP follows $1/z^2$ dependence.

Our previous studies showed that the kinetic spectrum of ions from CO_2 LPP is shifted to the higher energy side compared to a Nd:YAG LPP, and the estimated average charge state for CO_2 and Nd:YAG LPPs were 8 and 14, respectively.[23] It is well known that the propagation velocities of ions in a plasma are governed by space-charge effects, where highly charged ions possess higher velocities.[55] However, as mentioned earlier, the major species that contribute to visible

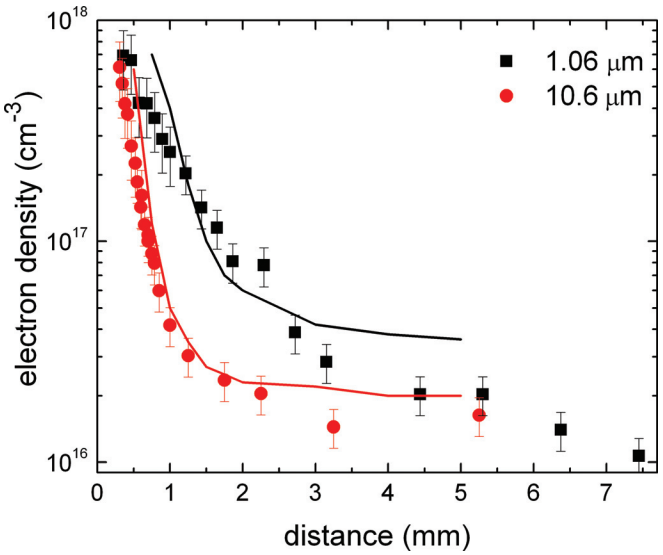

FIG. 9. (Color online) Spatial evolution of density of Nd:YAG and CO_2 produced plasma. Time integrated Stark broadened profiles were used for obtaining the density. The smooth curves in the figure represent the HEIGHTS estimate.

Downloaded 30 Mar 2011 to 128.46.102.183. Redistribution subject to AIP license or copyright; see http://jap.aip.org/about/rights_and_permissions

emissions are neutral and singly ionized species which are produced during the recombination expansion phase.

The emission features from a Nd:YAG LPP were found to be considerably extended in the plume expansion direction compared to a CO_2 LPP (Fig. 8). In the adiabatic expansive cooling regime, the particle loss is mainly due to collisional three-body recombination and radiative recombination. For conservation of energy, both the processes are accompanied by a third body; a photon for radiative and an electron for three-body recombination. The rates for three-body (R_c) and radiative (R_r) recombination are related to density and temperature of the plasma through[45]

$$R_c = -9.2 \times 10^{-39} Z^3 \ln \sqrt{Z^2 + 1} T_e^{-9/2} n_e^2 n_i, \quad (8)$$

$$R_r = -2.7 \times 10^{-19} Z^2 T_e^{-3/4} n_e n_i, \quad (9)$$

where T_e is in eV and n_e is in m^{-3}. From Eqs. (8) and (9), the three-body recombination will dominate over radiative recombination if

$$n_e \geq \frac{3 \times 10^{19} T_e^{15/4}}{Z} m^{-3}. \quad (10)$$

The above equation shows that radiative recombination assists particle loss only during the laser pulse, when the density and temperature are high. In the adiabatic expansion regime, the three-body recombination eventually dominates. The rate equations show that rate of collisional three-body recombination is proportional to the square of the density. Hence, one can expect the rate of three-body recombination will be considerably higher for plasmas produced by a 1.06 μm laser, leading to an extended visible emission from these plasmas, as seen in Fig. 8. Conversely, the lower rate of recombination effects in the CO_2 LPP results in the preservation of highly charged species and they move faster due to the space charge effects.

V. CONCLUSIONS

We investigated the effects of laser excitation wavelengths on Sn plasma properties. Sn plasmas are generated by exciting planar targets kept in vacuum using either 10.6 μm CO_2 laser or 1.06 μm Nd:YAG laser excitation. Currently, both CO_2 and Nd:YAG are considered as potential laser candidates for producing light sources for EUV lithography. Numerical modeling using HEIGHTS package showed that plasmas produced by both lasers, with an order of magnitude difference in power density, possess similar temperatures ~30–50 eV which is an ideal temperature for generating the required spectral emission in the in-band region. Our studies indicated that the major difference in plasma properties between Nd:YAG and CO_2 LPP are in their density evolution, both in space and time. The densities of the plasmas dictate the laser-plasma coupling and opacity and hence radiation transport. We employed interferometry and optical emission spectroscopy for estimating the density at various distances from the target surface as well as at different times during the isothermal and adiabatic plasma expansion regime and compared with modeling results.

Interferometry studies showed Nd:YAG produced plasmas reached critical density region of the probe beam and obscured the fringe visibility closer to the target surface (<100 μm). However, the estimated peak density of Nd:YAG LPP is $4.5 \times 10^{20}/cm^{-3}$ which is about an order less than the critical density of the probe beam. This indicates that when the plasma density approaches the critical density, refraction and opacity effects significantly limit the density measurements using interferometry. So the upper limit of density measurement in our interferometer setup is approximately 0.1 n_c. The estimated maximum density of CO_2 LPP is $5.5 \times 10^{19}/cm^3$ which is about 0.01 n_c and hence density information very close to target is obtainable. Density measurement in the isothermal expansion regime showed that the laser absorption front of the CO_2 LPP moved away from the target and hence most of the heating happened in the coronal regime. This indicates that most of the heating laser pulse is deposited efficiently in the plasma for CO_2 LPP instead of depositing at steep density profile observed with Nd:YAG LPP. This could also lead to efficient heating of the plasma and explains the observation of higher CE for CO_2 LPP even with more than an order of magnitude less laser irradiance levels. The results obtained with HEIGHTS simulation showed good agreement with the experimentally measured density values.

The density evolution at later times of plasma evolution and farther distances from the target were estimated using optical emission spectroscopy. Stark broadening of isolated Sn^+ emission was employed for deducing the electron density during plasma adiabatic expansion regime. The 2D spectral imaging method provided a very high spatial resolution of the Stark broadened profile in the plume expansion direction. An asymmetry in the emission spectral profile is noticed at distances < 1 mm from the target surface caused by ion micro-fields. An estimate of ion-induced asymmetries in the Stark broadened profiles showed it could introduce up to 20% error in the measured electron density values. However, the recorded density profiles followed Lorenzian line shapes at farther distances (>1 mm). This highlights that the Stark broadening cannot predict the LPP density accurately at short distances and earlier times. Densities of the plasmas produced by Nd:YAG and CO_2 lasers drop rapidly away from the target, however, the density decay is found to be much faster in the case of CO_2 laser. The spatial dependence of electron density for 1.06 μm excitation follows ~1/z dependence, while the CO_2 LPP follows $1/z^2$ dependence. The density estimate also showed that the measured values are considerably higher for 1.06 μm LPP at any spatial point during plasma evolution compared to 10.6 μm LPP. Hence, more three-body recombination noticed for 1.06 μm LPP leading to more out of band emission as well as broad UTA and ion kinetic energy distribution.

ACKNOWLEDGMENTS

This work is partially supported by School of Engineering, Purdue University.

[1]S. Amoruso, B. Toftmann, and J. Schou, Phys. Rev. E **69**, 056403 (2004).
[2]A. Bogaerts and Z. Y. Chen, Spectrochim. Acta B **60**, 1280 (2005).
[3]R. K. Singh and J. Narayan, Phys. Rev. B **41**, 8843 (1990).

Downloaded 30 Mar 2011 to 128.46.102.183. Redistribution subject to AIP license or copyright; see http://jap.aip.org/about/rights_and_permissions

[4]D. B. Chrisey and G. K. Hubler, *Pulsed Laser Deposition of Thin Films* (Wiley, New York, 1994).
[5]D. E. Motaung, M. K. Moodley, E. Manikandan, and N. J. Coville, J. Appl. Phys. **107**, 044308 (2010).
[6]V. Bakshi, *EUV Lithography* (SPIE Press, New York, 2009).
[7]D. Attwood, *Soft X-rays and EUV Radiation: Principles and Applications* (Cambridge, New York, 2000).
[8]S. Eliezer and K. Mima, *Applications of Laser-Plasma Interactions* (Taylor and Francis, Florida, 2008).
[9]B. C. Windom and D. W. Hahn, J. Anal. Atom. Spectrom. **24**, 1665 (2009).
[10]B. Fernandez, F. Claverie, C. Pecheyran, and O. F. X. Donard, Trac-Trends Anal. Chem. **26**, 951 (2007).
[11]P. Hough, C. McLoughlin, S. S. Harilal, J. P. Mosnier, and J. T. Costello, J. Appl. Phys. **107**, 024904 (2010).
[12]H. R. Griem, *Principles of Plasma Spectroscopy* (Cambridge, New York, 1997).
[13]B. Wu and A. Kumar, *EUV Lithography* (McGraw-Hill, New York, 2009).
[14]J. White, P. Dunne, P. Hayden, F. O'Reilly, and G. O'Sullivan, Appl. Phys. Lett. **90**, 181502 (2007).
[15]A. Hassanein, T. Sizyuk, S. S. Harilal, and T. Sizyuk, Proc. SPIE **7636**, 76360A (2010).
[16]Y. Tao, M. S. Tillack, S. S. Harilal, K. L. Sequoia, and F. Najmabadi, J. Appl. Phys. **101**, 023305 (2007).
[17]A. Nagano, T. Mochizuki, S. Miyamoto, and S. Amano, Appl. Phys. Lett. **93**, 091502 (2008).
[18]S. A. George, W. T. Silfvast, K. Takenoshita, R. T. Bernath, C. S. Koay, G. Shimkaveg, and M. C. Richardson, Opt. Lett. **32**, 997 (2007).
[19]S. S. Harilal, B. O'Shay, M. S. Tillack, and Y. Tao, J. Phys. D **39**, 484 (2006).
[20]S. S. Harilal, M. S. Tillack, B. O'Shay, Y. Tao, and A. Nikroo, Opt. Lett. **31**, 1549 (2006).
[21]S. S. Harilal, B. O'Shay, Y. Tao, and M. S. Tillack, Appl. Phys. B **86**, 547 (2007).
[22]D. Campos, S. S. Harilal, and A. Hassanein, J. Appl. Phys. **108**, 113305 (2010).
[23]D. Campos, S. S. Harilal, and A. Hassanein, Appl. Phys. Lett. **96**, 151501 (2010).
[24]S. S. Harilal, R. W. Coons, P. Hough, and A. Hassanein, Appl. Phys. Lett. **95**, 221501 (2009).
[25]A. Hassanein, V. Sizyuk, T. Sizyuk, and S. Harilal, Journal of Micro/Nanolithography Mems and Moems **8**, 041503 (2009).
[26]I. H. Hutchinson, *Principles of Plasma Diagnostics* (Cambridge University Press, New York, 1987).
[27]S. S. Harilal, B. O'Shay, M. S. Tillack, and M. V. Mathew, J. Appl. Phys. **98**, 013306 (2005).
[28]P. Hough, C. McLoughlin, T. J. Kelly, S. S. Harilal, J. P. Mosnier, and J. T. Costello, Appl. Surf. Sci. **255**, 5167 (2009).
[29]A. Kumar, R. K. Singh, J. Thomas, and S. Sunil, J. Appl. Phys. **106**, 043306 (2009).
[30]A. Hassanein, V. Sizyuk, V. Tolkach, V. Morozov, and B. Rice, Journal of Microlithography, Microfabrication & Microsystems **3**, 130 (2004).
[31]V. Sizyuk, A. Hassanein, V. Morozov, and T. Sizyuk, "Heights Integrated Model as Instrument for Simulation of Hydrodynamic, Radiation Transport, and Heat Conduction Phenomena of Laser-Produced Plasma in EUV Applications," Argonne National Laboratory Report, ANL MCS CPH 06/56 (2007).
[32]G. Cisneros, J. S. Helman, and C. N. J. Wagner, Phys. Rev. B **25**, 4248 (1982).
[33]J. P. Petrakian, A. R. Cathers, J. E. Parks, R. A. Macrae, T. A. Callcott, and E. T. Arakawa, Phys. Rev. B **21**, 3043 (1980).
[34]G. G. Grigoryan, A. G. Leonov, E. A. Manykin, A. A. Rudenko, M. G. Sitnikov, and A. N. Starostin, J. Exp. Theor. Phys. **97**, 678 (2003).
[35]L. Frommhold, Collisional-Induced Absorption in Gases (Cambridge Univ. Press, Cambridge, 1993).
[36]T. W. Johnston and J. M. Dawson, Phys. Fluids **16**, 722 (1973).
[37]A. M. Hassanein, G. L. Kulcinski, and W. G. Wolfer, Nuclear Engineering and Design-Fusion **1**, 307 (1984).
[38]R. W. Coons, D. Campos, S. S. Harilal, and A. Hassanein, J. Appl. Phys. **108**, 063306 (2010).
[39]N. Hurst and S. S. Harilal, Rev. Sci. Instrum. **80**, 035101 (2009).
[40]P. Hough, T. J. Kelly, C. McLoughlin, S. S. Harilal, J. P. Mosnier, and J. T. Costello, J. Phys. D **42**, 055211 (2009).
[41]http://www.optics.tugraz.at/idea/idea.html for "IDEA - Interferometric Data Evaluation Algorithms."
[42]R. A. Burdt, S. Yuspeh, K. L. Sequoia, Y. Z. Tao, M. S. Tillack, and F. Najmabadi, J. Appl. Phys. **106**, 033310 (2009).
[43]H. Tanaka, A. Matsumoto, K. Akinaga, A. Takahashi, and T. Okada, Appl. Phys. Lett. **87**, 041503 (2005).
[44]Y. B. Zeldovich and Y. P. Raizer, *Physics of Shock Waves and High-Temperature Hydrodynamic Phenomena* (Dover, New York, 2001).
[45]P. T. Rumsby and J. W. M. Paul, Plasma Phys. Controlled Fusion **16**, 247 (1974).
[46]C. Aragon and J. A. Aguilera, Spectrochim. Acta B **63**, 893 (2008).
[47]J. Hoffman, W. Mroz, A. Prokopiuk, and Z. Szymanski, Appl. Phys. A **92**, 921 (2008).
[48]H. R. Griem, *Plasma Spectroscopy* (McGraw-Hill, New York, 1964).
[49]C. Colon, G. Hatem, E. Verdugo, P. Ruiz, and J. Campos, J. Appl. Phys. **73**, 4752 (1993).
[50]M. Milaen and J. J. Laserna, Spectrochim. Acta B **56**, 275 (2001).
[51]A. Alonso-Medina and C. Colon, Astrophys. J. **672**, 1286 (2008).
[52]N. Konjevic, Phys. Rep. **316**, 339 (1999).
[53]R. F. Joyce, L. A. Woltz, and C. F. Hooper, Phys. Rev. A **35**, 2228 (1987).
[54]J. Bengoechea, C. Aragon, and J. A. Aguilera, Spectrochim. Acta B **60**, 897 (2005).
[55]O. Morris, A. O'Connor, E. Sokell, and P. Dunne, Plasma Sour. Sci. Technol. **19**, 025007 (2010).

Downloaded 30 Mar 2011 to 128.46.102.183. Redistribution subject to AIP license or copyright; see http://jap.aip.org/about/rights_and_permissions